JACS
JOURNAL OF THE AMERICAN CHEMICAL SOCIETY
Article
pubs.acs.org/JACS

Fast Photoelectron Transfer in (C_{ring})−C_3N_4 Plane Heterostructural Nanosheets for Overall Water Splitting

Wei Che,[†] Weiren Cheng,[†] Tao Yao, Fumin Tang, Wei Liu, Hui Su, Yuanyuan Huang, Qinghua Liu,* Jinkun Liu, Fengchun Hu, Zhiyun Pan, Zhihu Sun, and Shiqiang Wei*

National Synchrotron Radiation Laboratory, University of Science and Technology of China, Hefei, 230029 Anhui, PR China

Supporting Information

ABSTRACT: Direct and efficient photocatalytic water splitting is critical for sustainable conversion and storage of renewable solar energy. Here, we propose a conceptual design of two-dimensional C_3N_4-based in-plane heterostructure to achieve fast spatial transfer of photoexcited electrons for realizing highly efficient and spontaneous overall water splitting. This unique plane heterostructural carbon ring (C_{ring})−C_3N_4 nanosheet can synchronously expedite electron−hole pair separation and promote photoelectron transport through the local in-plane π-conjugated electric field, synergistically elongating the photocarrier diffusion length and lifetime by 10 times relative to those achieved with pristine g-C_3N_4. As a result, the in-plane (C_{ring})−C_3N_4 heterostructure could efficiently split pure water under light irradiation with prominent H_2 production rate up to 371 μmol g^{-1} h^{-1} and a notable quantum yield of 5% at 420 nm.

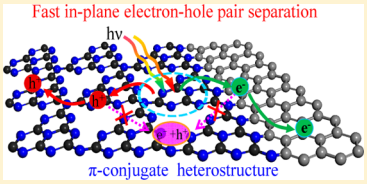

INTRODUCTION

Effectively storing renewable solar energy in chemical form has been widely recognized as a promising and sustainable strategy to meet future worldwide energy demand.[1−3] To achieve this goal, the use of abundant sunlight to directly split water into H_2 and O_2 is a potentially scalable approach.[4−6] As is well-known, the vivid solar water splitting process sequentially undergoes three steps: light harvest, photocarrier separation/transport, and surface redox. Unfortunately, direct and efficient photocatalytic water splitting encounters great challenges of sluggish photocarrier transfer during long-distance transportation, leading to notorious photocarriers' recombination.[7−9] To improve the solar conversion efficiency, it is thus highly imperative to accelerate the photocarrier transfer kinetics to realize fast spatial separation of the photoexcited electron−hole pairs by developing novel material or employing new structural design.

To date, various approaches have been devoted to modifying the atomic and electronic structure of photocatalysts via element doping or heterojunction construction to accelerate electron−hole separation and transportation. As a classical modification, element doping has been generally demonstrated to significantly reduce charge transfer barrier and then effectively accelerate photocarrier separation in TiO_2 and Fe_2O_3 photocatalysts, yet also engenders external energy loss due to the newcoming carrier recombination centers.[10−12] To overcome this issue, van der Waals heterostructures stacked by various two-dimensional ultrathin functional nanosheets such as MoS_2/graphene and $SnSe_2$/WSe_2 have been sought to simultaneously promote the charge transfer and suppress the photoexcited electron−hole recombination in bulk materials.[13,14] Unfortunately, obvious photocarrier recombination in the interlaminar space region still occurs due to the interlayer weak van der Waals driving force.[15,16] Recently, two-dimensional layered semiconductor materials with earth abundant elements and favorable band gap, such as graphitic carbon nitride (g-C_3N_4), have been regarded as effective photocatalysts for direct solar water splitting owing to the shortened photocarrier transportation distance.[17,18] Indeed, significant progress has been achieved on the metal-free g-C_3N_4 based photocatalysts for improved solar water splitting activity via C-dots deposition and so on.[19−24] Even so, for more effective and fast charge carrier transfer, it is essentially necessary to induce an intrinsic driving force in the two-dimensional semiconductor plane for delocalization of the photocarrier around the photoexcited sites. Consequently, a strong in-building electric field induced by in-plane heterostructure with different work function is urgently needed to overcome this limitation and would automatically guide ordered movement of photocarrier to suitable redox sites.[25,26] In particular, seamlessly stitching two-dimensional domains in-plane with the similar aromatic structures such as a graphitic carbon ring (C_{ring}) section via continuous π-conjugated bond could effectively tune the band structure and electronic transport property, resulting in unimpeded in-plane electron−hole separation and charge transfer.[17,27,28]

To maximize solar-energy conversion efficiency, herein, we conceptually design an in-plane π-conjugated heterostructure via intimately connecting two-dimensional domains with different electron affinity, to synergistically extend the light-absorption and promote the electron−hole pair separation and transportation (Figure 1a). Our proof-of-concept demonstration is based on the use of the metal-free layered graphitic carbon nitride (g-C_3N_4) as photocatalyst due to the suitable band positions and strong in-plane π-conjugated bonds.[29,30]

Received: November 17, 2016
Published: February 13, 2017

DOI: 10.1021/jacs.6b11878
J. Am. Chem. Soc. 2017, 139, 3021−3026

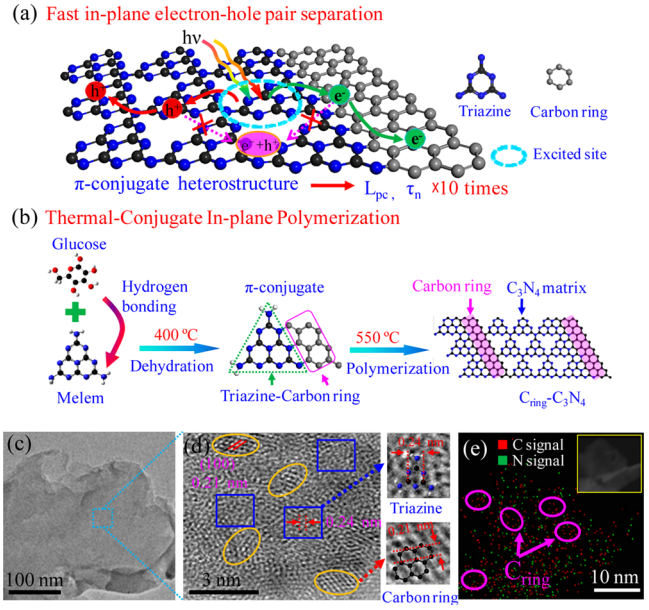

Figure 1. (a) Schematic for photocarrier transfer in $(C_{ring})-C_3N_4$, where L_{pc} and τ_n represent the photocarrier diffusion length and lifetime, respectively. (b) Synthetic route for the in-plane heterostructure of $(C_{ring})-C_3N_4$. (c) TEM image and (d) HRTEM image for the sample. The elliptic area represents carbon ring, and the rectangular area is C_3N_4 matrix. (e) EDS mapping of $(C_{ring})-C_3N_4$. The inset of TEM image shows the corresponding region for mapping.

Moreover the N pots with rich lone-pair electrons at the edge of tri-*s*-triazine rings provide ideal sites for interfacial connection of heterostructure,[31,32] especially for a similar micro-π-conjugated unit such as carbon ring. The homogeneous sp^2-hybridized π-conjugated bonding of carbon ring in the $(C_{ring})-C_3N_4$ plane heterostructure could quickly trap photoexcited electrons and drive them to suitable active sites in a local micro-π-conjugated connection unit, dramatically enhancing the photocarrier separation efficiency (Figure 1a). The high electron state density around the Fermi level introduced by carbon ring incorporation could synergistically prolong the photocarrier diffusion length and lifetime significantly by 10 times relative to those of pristine g-C_3N_4. Hence, the novel $(C_{ring})-C_3N_4$ in-plane heterostructure exhibits highly efficient water splitting activity under light irradiation with prominent H_2 production rate up to 371 μmol g^{-1} h^{-1} and a notable quantum yield of 5% at 420 nm.

RESULTS AND DISCUSSION

The in-plane g-C_3N_4-based heterostructure was synthesized by a thermal-conjugate strategy as depicted schematically in Figure 1b. The key in the synthesis is the planar π-conjugate coalescence between the heterogeneous domains. Because of the similar aromatic structure, the in-plane connection is realized by the sp^2-hybridized C−N bonds between the carbon ring-contained glucose molecule and the melem unit through dehydration reaction under the mild temperature of 400 °C. After that, the triazine carbon ring motif is further polymerized to the final in-plane g-C_3N_4-based heterostructure via π-conjugate bonds under 550 °C. The as-synthesized g-C_3N_4 plane heterostructural nanosheets incorporated with in-plane carbon ring (denoted as $(C_{ring})-C_3N_4$ hereafter) can be verified by transmission electron microscopy (TEM) and high-resolution TEM (HRTEM) (Figure 1c,d). As illustrated in the TEM image, homogeneous sheet-like $(C_{ring})-C_3N_4$ is observed, which exhibits a smooth surface without any obvious nanoparticle growth. The HRTEM image displays lots of

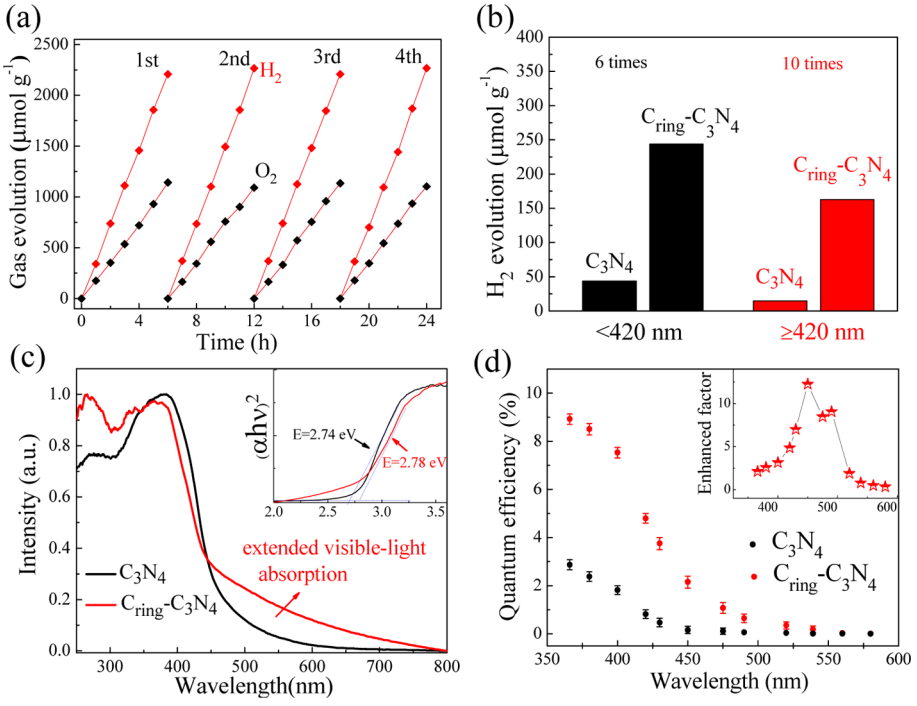

Figure 2. (a) Typical time course of H_2 and O_2 evolution for $(C_{ring})-C_3N_4$. (b) H_2 evolution under UV (<420 nm) and visible light (≥420 nm) per hour. (c) UV−visible absorption and corresponding Tauc/Davis-Mott plots. (d) Photocatalytic quantum efficiency and corresponding enhanced factor. For suspension photocatalystic water splitting testing, ~3 wt % Pt H_2PtCl_6 solution was added in aqueous solution without any sacrificial reagents.

DOI: 10.1021/jacs.6b11878
J. Am. Chem. Soc. 2017, 139, 3021−3026

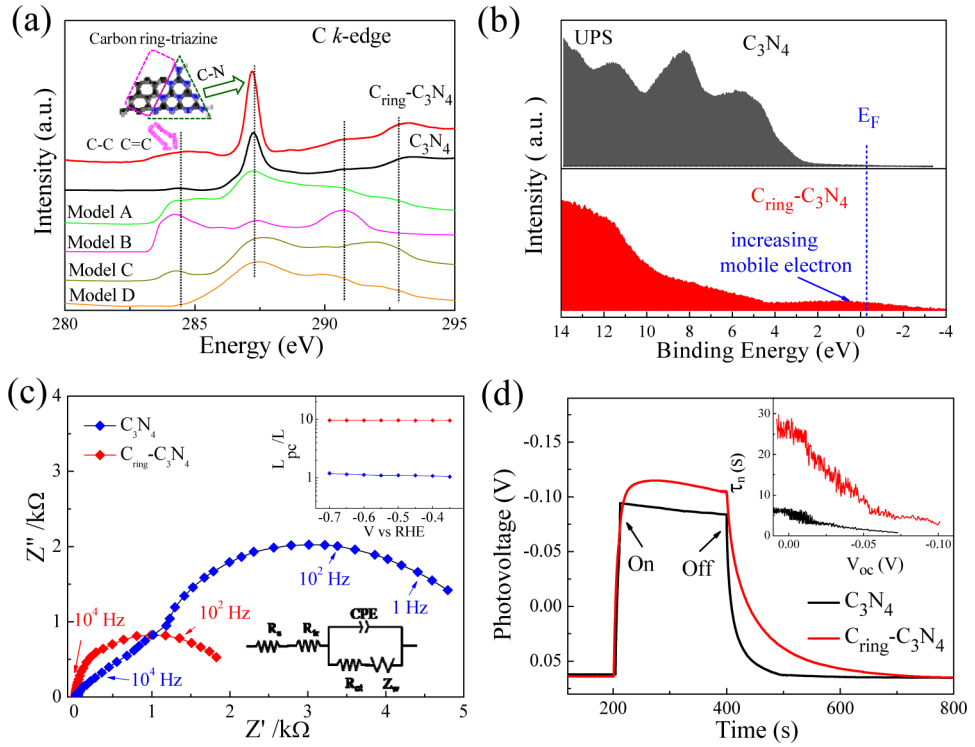

Figure 3. (a) C *K*-edge XANES experimental and theoretical spectra, where models A–D correspond to in-plane (C_{ring})–C_3N_4 heterostructure, mixed carbon ring and C_3N_4, C-doping C_3N_4, and pure C_3N_4, respectively. (b) UPS spectra. (c) Electrochemical impedance spectra (EIS) and insets show the equivalent circuit impedance model and the calculated photocarrier diffusion length. (d) Transient OCVD measurement and inset shows the average lifetimes of the photogenerated carriers (τ_n) obtained from the OCVD measurement.

distinct lattice fringe regions (orange ellipses in Figure 1d) randomly incorporated in the disordered basal plane domain of g-C_3N_4. The corresponding lattice fringes of 0.21 nm can be ascribed to the (100) planes of graphite which is obviously smaller than the characteristic in-plane *d*-space distance of 0.24 nm in g-C_3N_4 (right panel of Figure 1d). Seen from Figure 1e, both C and N signals are detected in the (C_{ring})–C_3N_4 nanosheet, originating from C_3N_4 domains, but for the marked elliptic region, evident enrichment of C is observed. Considering the absence of carbon dots or other carbon impurity, these enriched C signals can be ascribed to the presence of in-plane carbon ring. Moreover, the (C_{ring})–C_3N_4 still maintains the primary structural features of g-C_3N_4 after the incorporation of carbon ring as confirmed by the X-ray diffraction patterns (Figure S7). These results evidently demonstrate the successful formation of in-plane g-C_3N_4 based heterostructure with carbon ring embedded in the basal plane of g-C_3N_4.

To examine the photocatalytic activity, we evaluated the water splitting performance of (C_{ring})–C_3N_4 suspension in pure water without any sacrificial reagents under standard reaction and measurement conditions. The typical time course of gas evolution over the (C_{ring})–C_3N_4 is shown in Figure 2a. Notably, simultaneous evolution of H_2 and O_2 gases in a stoichiometric ratio of 2:1 was obtained for (C_{ring})–C_3N_4, and the corresponding constant H_2 and O_2 evolution rates are up to 371 and 184 μmol g^{-1} h^{-1}, respectively. It is of particular note that the photocatalytic H_2 evolution rate of the sample under visible light (≥420 nm) irradiation was up to 150 μmol g^{-1} h^{-1} (see Figure 2b), increased by 10 times in comparison with that (12 μmol g^{-1} h^{-1}) of pristine g-C_3N_4. To further confirm the superior visible-light photocatalytic activity, the light absorption property and photocatalytic quantum efficiency of (C_{ring})–C_3N_4 were measured. As seen from Figure 2c, the absorption edges of both (C_{ring})–C_3N_4 and C_3N_4 are around 460 nm, and a good linear fit is observed when using $(\alpha h\nu)^2$ for Tauc plots, indicating direct bandgap semiconductors for both C_3N_4 and (C_{ring})–C_3N_4.[19] The accurate band gap of (C_{ring})–C_3N_4 is determined to be 2.78 eV, very close to that (2.74 eV) of pristine g-C_3N_4 (see the inset in Figure 2c). Interestingly, there is an extended visible-light absorption over 500–800 nm for (C_{ring})–C_3N_4, which enables the possible utilization of low-energy visible light. As seen from the quantum efficiency measurement results (Figure 2d), the quantum efficiency of (C_{ring})–C_3N_4 reaches up to 5% at 420 nm and remains at 1% at 500 nm, an order of magnitude enhancement over 420–500 nm relative to that of pristine g-C_3N_4 (inset in Figure 2d). In sharp contrast, the quantum efficiency of pristine g-C_3N_4 is much lower in both the UV and visible-light regions, below 1% at 420 nm and fast decreased to zero beyond 450 nm. Meanwhile, the (C_{ring})–C_3N_4 maintains a high rate of H_2 and O_2 evolution (ca. 150 and 74 μmol g^{-1} h^{-1}, respectively) with robust stability when recycled 60 times (Figure S12). Therefore, all the above results demonstrate that the (C_{ring})–C_3N_4 as a promising and efficient photocatalyst possesses excellent photocatalytic activity as well as long-term stability for direct water splitting.

To understand the origin of the prominent photocatalytic activity of (C_{ring})–C_3N_4, we performed various atomic and electronic structural characterizations on the samples. The X-ray absorption near-edge spectroscopy (XANES), exceptionally sensitive to the local electronic configuration,[30] was used to further identify the heterostructure of (C_{ring})–C_3N_4. As seen in Figure 3a, the XANES spectrum of (C_{ring})–C_3N_4 displays an

DOI: 10.1021/jacs.6b11878
J. Am. Chem. Soc. 2017, 139, 3021–3026

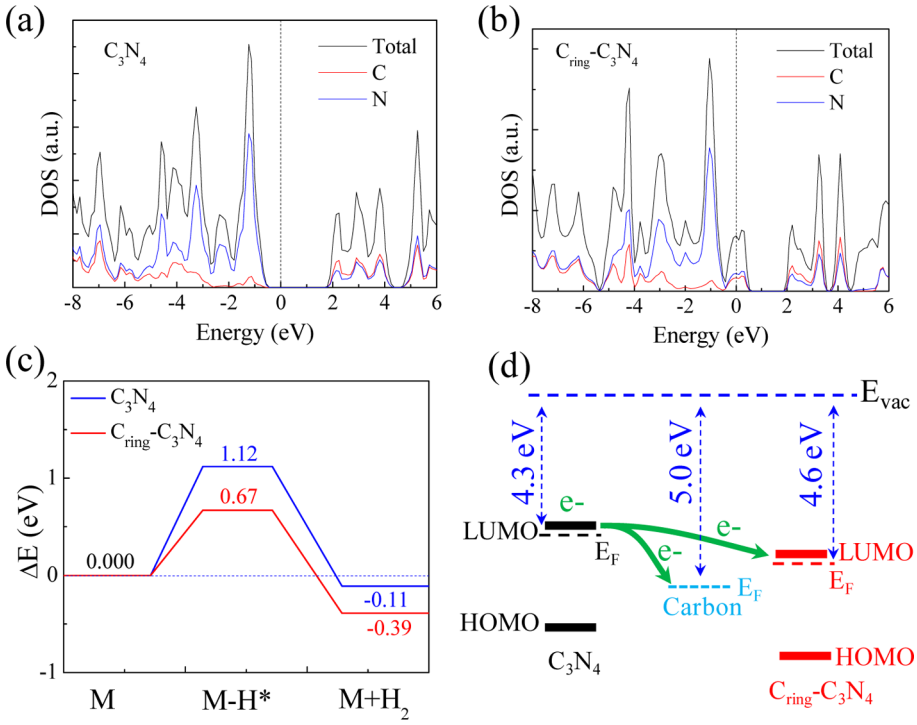

Figure 4. Calculated band structure and Fermi level profile for samples. (a, b) Calculated DOSs for pristine g-C_3N_4 and (C_{ring})−C_3N_4. (c) Calculated adsorption energy profiles for pristine g-C_3N_4 and (C_{ring})−C_3N_4 where M refers to surface C sites. (d) Fermi energy level profile for pristine g-C_3N_4, carbon, and (C_{ring})−C_3N_4.

obvious broad peak with enhanced intensity over 283−285 eV, ascribed to sp^2 hybridization of C−C and C═C bonds for graphitic carbon ring.[33,34] To further support this deduction, theoretical C *K*-edge XANES spectra for several structure models calculated using FEFE8.2 code are also shown in Figure 3a. Apparently, the calculations based on (C_{ring})−C_3N_4 models (Model A) could reproduce the main spectral features of the corresponding experimental spectra of (C_{ring})−C_3N_4, providing solid theoretical evidence for the formation of sp^2 π-conjugated heterointerface in (C_{ring})−C_3N_4. This π-conjugate connection will significantly modify the electronic structure of in-plane heterostructure.

The ultraviolet photoelectron spectra (UPS) shown in Figure 3b display a significant electron density distribution at the Fermi level for (C_{ring})−C_3N_4, inferring evident increase of charge density upon carbon ring incorporation. Furthermore, according to the slope of Mott−Schottky plots (Figure S13), the carrier density of the (C_{ring})−C_3N_4 is dramatically enhanced by 1 order of magnitude with the slightly positive shift of the flat-band potentials (~1.0 eV versus RHE) relative to that of pristine C_3N_4. Taking the band gap into consideration, the valence band and conduction band edge level of (C_{ring})−C_3N_4 are located at around 1.6 and −1.1 eV vs RHE, respectively, which enables the direct photocatalytic splitting of pure water.[35,36] Because of the increased charge density, the photocarrier transfer barrier of (C_{ring})−C_3N_4 is significantly reduced as confirmed by the electrochemical impedance measurement (Figure 3c). More importantly, their calculated photocarrier diffusion lengths (L_{pc}/L) are dramatically enhanced by 10 times compared with that of pristine g-C_3N_4, inferring tremendously accelerated photocarrier transfer kinetics. Moreover, the second electron emission (SEE) spectra (Figure S13) reveal that the work function of (C_{ring})−C_3N_4 is elevated to 4.60 eV, 0.3 eV higher than that of pristine g-C_3N_4 and close to the reported value of graphite (5 eV).[36,37] Benefitting from the increased mobile electrons and higher work function, (C_{ring})−C_3N_4 can more effectively trap photoexcited electrons and suppress electron−hole recombination than pristine g-C_3N_4. This can be further confirmed by the transient open-circuit voltage decay (OCVD) measurements shown in Figure 3d. The (C_{ring})−C_3N_4 holds higher open-circuit voltage and exhibits slower photovoltage decay behavior after light turning on or off, corresponding to higher energetic and longer lifetime of photoexcited carrier. It is readily seen from the inset of Figure 3d that the average lifetimes of photocarrier in (C_{ring})−C_3N_4 are substantially prolonged by nearly an order of magnitude relative to that of pristine g-C_3N_4. This indicates the highly efficient electron−hole pair separation, consistent with the smooth transient photocurrent curve and strength reduction of photoluminescence emission (PL) feature for (C_{ring})−C_3N_4 (Figure S14). Combining the above results, we consider that the electron structure of (C_{ring})−C_3N_4 has been greatly modified by the in-plane incorporated carbon ring, leading to efficient photoexcited electron−hole separation and longer photocarrier lifetime.

For an in-depth understanding of the relationship between the in-plane heterostructure and photocatalytic activity, the first-principles calculations of energy and band structure were performed. It can be clearly seen that electron densities of states (DOS) for pristine g-C_3N_4 present a semiconductor character, and the Fermi level is located within the middle of the band gap without any electron distribution around the Fermi level (Figure 4a).[17,26] In contrast, for (C_{ring})−C_3N_4, an intermediate state is introduced into the energy gap, with the Fermi level across the band gap state, in good agreement with the UPS (Figure 3b) and UV−visible absorption (Figure 2c) results. The new intermediate energy level is located at ~0.5 eV above the valence band; meanwhile, the conduction band edge

DOI: 10.1021/jacs.6b11878
J. Am. Chem. Soc. 2017, 139, 3021−3026

of $(C_{ring})-C_3N_4$ is positively shifted by 0.2 eV relative to that of pristine g-C_3N_4. The narrowed band gap of $(C_{ring})-C_3N_4$ corresponds to expanded visible light absorption and lowered overpotential of reduction reaction. This electronic property with large amount of mobile electron around the Fermi level would greatly increase the adsorption energy of water molecule and decrease the energy barrier for the intermediate formation during photocatalytic water splitting process. Evidently, the surface N sites in $(C_{ring})-C_3N_4$ possess larger H_2O adsorption energy of 1.10 eV, obviously higher than that of pristine g-C_3N_4 (0.9 eV). Furthermore, the energy barrier of H* adsorbed at the surface of $(C_{ring})-C_3N_4$ is remarkably reduced by 0.45 eV compared to that of pristine g-C_3N_4 (Table S2).

Summarizing all the above results, the in-plane heterostructure of $(C_{ring})-C_3N_4$ is a promising photocatalyst which successfully splits pure water into H_2 and O_2 without sacrificial reagents under light irradiation. The H_2 production rate of $(C_{ring})-C_3N_4$ is high up to 150 μmol g^{-1} h^{-1} upon irradiation of visible light (≥420 nm) with a notable quantum yield of 5% at 420 nm. More importantly, the in-plane $(C_{ring})-C_3N_4$ heterostructural nanosheets display significantly higher photocatalytic water splitting activity than most of photocatalysts, with hydrogen evolution rate up to 371 μmol h^{-1} g^{-1} under full solar spectrum (see Table S1).[38,39] This intrinsic photocatalytic activity is stemmed from the π-conjugated $(C_{ring})-C_3N_4$ plane-heterostructure. Such strong sp^2-hybridized electronic structure features with rich free electron around the Fermi level play critical roles in suppression of photoexcited electron−hole recombination and enhancement of visible-light utilization. First, the interaction coupling of in-plane carbon ring and triazine unit creates a new intermediate energy level above the valence band, providing a novel transfer path for visible light with lower energy,[40,41] as verified by UV−visible absorption spectrum and DOS results. Moreover, the positive shift of conduction band edge, mainly composed by C 2p, lower the overpotential of the surface reduction. Second, the interfacial charge gradient in this micro-π-conjugated heterointerface caused by different work functions of domains results in gradient charge potential level (Figure 4d). This gradient level could automatically drive electron−hole pair separation in opposite directions and move the photocarriers to suitable reactive sites (Figure 1a). Thereby, the unique carbon-ring−triazine unit can be regarded as a small redox cell for water splitting, greatly shortening the transfer distance and dramatically increasing the spatial separation efficiency of photoexcited electron−hole pair as demonstrated by OCVD measurement results. Finally, the increased mobile electron together with improved work function significantly modifies the surface property of $(C_{ring})-C_3N_4$ with strong electrophilicity, which can greatly promote the surface adsorption and reduction of H^+ and thereby effectively avoid surface electron−hole recombination as attested by the transient current and PL measurement results (Figure S14). Indeed, our first-principles energy calculations confirm that the energy barrier of H* formation and H_2 desorption for $(C_{ring})-C_3N_4$ is clearly decreased to 0.67 and −0.39 eV from 1.12 and −0.11 eV, respectively, thus resulting in the acceleration of surface reaction kinetics.

CONCLUSION

In summary, we have designed a novel in-plane heterostructure based on g-C_3N_4 and graphitic carbon ring to efficiently separate the photoexcited electron−hole pair and facilitate the photocarrier's transportation for direct photocatalytic water splitting. The diffusion length and lifetime of photocarrier are significantly increased by 10 times relative to those of pristine g-C_3N_4, and the plane heterostructural nanosheets of $(C_{ring})-C_3N_4$ can effectively split pure water under light irradiation with prominent H_2 production rate up to 371 μmol g^{-1} h^{-1} and a notable average quantum yield of 5% at 420 nm. Electronic structure characterization and density functional theory calculations reveal that the novel band structure of $(C_{ring})-C_3N_4$ in-plane heterostructure with significant electron density distribution near the Fermi level promotes the photoexcited electron−hole pair separation and transfer and accelerates the surface reaction kinetics for enhanced photocarrier utilization. Our results may open up opportunities for the design of efficient and cost-effective photocatalysts for the production of clean energy.

EXPERIMENTAL SECTION

Material Preparation. A multistep heating strategy was developed to synthesize the in-plane heterostructure $(C_{ring})-C_3N_4$ nanosheets. Specially, 10 g of melamine powder was completely dispersed into 50 mL of glucose solution under an ultrasonic bath at 50 °C for 30 min and then the mixed solution was dried in 60 °C drying baker for overnight to entirely remove water. After that, the mixed resultants sequentially went through three stages of heating to form the final product: 300 °C for 1h, 400 °C for 1 h, and 550 °C for 4 h. In comparison, graphite and pristine C_3N_4 were synthesized by the thermal treatment of glucose and melamine under 550 °C for 4 h, respectively. All graphite, pristine C_3N_4, and $(C_{ring})-C_3N_4$ are washed by DI water several times to completely remove residual species after the heating treatment. A post-purification treatment of the as-synthesized samples was carried out before the characterization and performance measurement (see more details in the Supporting Information).

Characterization. Transmission electron microscopy (TEM), high-resolution transmission electron microscopy (HRTEM), and energy dispersive X-ray spectra (EDS) analysis were performed on a JEM-2100F microscope at an acceleration voltage of 200 kV. The SEM measurements were conducted using a scanning electron microscope (JSM-6700F, 5 kV).The XRD patterns were performed on Philips X'Pert Pro Super X-ray diffractometer with Cu Kα radiation. The UV−vis spectra (DRS) were recorded on a Shimadzu DUV-3700 spectrophotometer. X-ray photoelectron spectra (XPS) were acquired on an ESCALAB MKII with Mg Kα ($h\nu$ = 1253.6 eV) as the excitation source. Photocatalytic overall water splitting reactions were carried out in a top-irradiation-type photoreactor (Pyrex glass) connected to a closed gas circulation system. The generated hydrogen and oxygen were measured via gas chromatograph (GC) equipped with a thermal conduction detector (TCD, 5 Å molecular sieve columns with 3 m length) using Ar as carrier gas with flow rate of 20 mL/min. Photoemission spectroscopy experiments were performed at the Catalysis and Surface Science Endstation at the BL11U beamline in the National Synchrotron Radiation Laboratory (NSRL). The beamline is connected to an undulator and equipped with two gratings that offer soft X-rays from 20 to 600 eV with a typical photon flux of 5×10^{10} photons/s and a resolution ($E/\Delta E$) better than 10^4 at 29 eV. The C and N *K*-edge X-ray absorption near-edge spectra (XANES) were measured at BL12B-a beamline of NSRL in the total electron yield (TEY) mode by collecting the sample drain current under a vacuum better than 5×10^{-8} Pa. The beam from the bending magnet was monochromatized utilizing a varied linespacing plane grating and refocused by a toroidal mirror. The energy range is 100−1000 eV with an energy resolution of ca. 0.1 eV.

DOI: 10.1021/jacs.6b11878
J. Am. Chem. Soc. 2017, 139, 3021−3026

■ ASSOCIATED CONTENT

Supporting Information

The Supporting Information is available free of charge on the ACS Publications website at DOI: 10.1021/jacs.6b11878.

Sample preparation and characterizations, TEM, SEM, AFM, XPS spectra, XRD patterns, EDS mapping, photocatalytic performance measurements of the samples, XANES measurement and data analysis, and density functional theory calculation details and analysis (PDF)

■ AUTHOR INFORMATION

Corresponding Authors

*E-mail: qhliu@ustc.edu.cn.
*E-mail: sqwei@ustc.edu.cn.

ORCID

Zhihu Sun: 0000-0002-3898-969X
Shiqiang Wei: 0000-0002-2052-1132

Author Contributions

†These authors contributed equally to this work.

Notes

The authors declare no competing financial interest.

■ ACKNOWLEDGMENTS

This work was supported by the National Natural Science Foundation of China (Grant Nos. 21533007, 11621063, U1532265, 21603207, 11435012, 11305174, and 11422547), and the Fundamental Research Funds for the Central Universities (WK2310000054), and the China Postdoctoral Science Foundation (2016M590581).

■ REFERENCES

(1) Kudo, A.; Miseki, Y. *Chem. Soc. Rev.* **2009**, *38*, 253−278.
(2) Wang, X. C.; Maeda, K.; Thomas, A.; Takanabe, K.; Xin, G.; Carlsson, J. M.; Domen, K.; Antonietti, M. *Nat. Mater.* **2009**, *8*, 76−80.
(3) Chen, X. B.; Shen, S. H.; Guo, L. J.; Mao, S. S. *Chem. Rev.* **2010**, *110*, 6503−6570.
(4) Tada, H.; Mitsui, T.; Kiyonaga, T.; Akita, T.; Tanaka, K. *Nat. Mater.* **2006**, *5*, 782−786.
(5) Kageshima, Y.; Shinagawa, T.; Kuwata, T.; Nakata, J.; Minegishi, T.; Takanabe, K.; Domen, K. *Sci. Rep.* **2016**, *6*, 24633.
(6) Liang, Y. H.; Sun, X. P.; Asiri, A. M.; He, Y. Q. *Nanotechnology* **2016**, *27*, 12LT01.
(7) Jiang, N.; You, B.; Sheng, M. L.; Sun, Y. J. *ChemCatChem* **2016**, *8*, 106−112.
(8) Soldat, J.; Busser, G. W.; Muhler, M.; Wark, M. *ChemCatChem* **2016**, *8*, 153−156.
(9) Wang, P.; Song, F.; Amal, R.; Ng, Y. H.; Hu, X. L. *ChemSusChem* **2016**, *9*, 472−477.
(10) Di Valentin, C.; Pacchioni, G. *Acc. Chem. Res.* **2014**, *47*, 3233−3241.
(11) Sivula, K.; Le Formal, F.; Gratzel, M. *ChemSusChem* **2011**, *4*, 432−449.
(12) Zhang, G. G.; Zhang, M. W.; Ye, X. X.; Qiu, X. Q.; Lin, S.; Wang, X. C. *Adv. Mater.* **2014**, *26*, 805−809.
(13) Deng, D. H.; Novoselov, K. S.; Fu, Q.; Zheng, N. F.; Tian, Z. Q.; Bao, X. H. *Nat. Nanotechnol.* **2016**, *11*, 218−230.
(14) Duan, X. D.; Wang, C.; Pan, A.; Yu, R. Q.; Duan, X. F. *Chem. Soc. Rev.* **2015**, *44*, 8859−8876.
(15) Hou, Y. D.; Laursen, A. B.; Zhang, J. S.; Zhang, G. G.; Zhu, Y. S.; Wang, X. C.; Dahl, S.; Chorkendorff, I. *Angew. Chem., Int. Ed.* **2013**, *52*, 3621−3625.
(16) Zhang, Y. J.; Mori, T.; Niu, L.; Ye, J. H. *Energy Environ. Sci.* **2011**, *4*, 4517−4521.
(17) Du, A. J.; Sanvito, S.; Li, Z.; Wang, D. W.; Jiao, Y.; Liao, T.; Sun, Q.; Ng, Y. H.; Zhu, Z. H.; Amal, R.; Smith, S. C. *J. Am. Chem. Soc.* **2012**, *134*, 4393−4397.
(18) Zhang, Z. Z.; Long, J. L.; Yang, L. F.; Chen, W. K.; Dai, W. X.; Fu, X. Z.; Wang, X. X. *Chem. Sci.* **2011**, *2*, 1826−1830.
(19) Liu, J.; Liu, Y.; Liu, N. Y.; Han, Y. Z.; Zhang, X.; Huang, H.; Lifshitz, Y.; Lee, S. T.; Zhong, J.; Kang, Z. H. *Science* **2015**, *347*, 970−974.
(20) Cui, Y. J.; Ding, Z. G.; Fu, X. Z.; Wang, X. C. *Angew. Chem., Int. Ed.* **2012**, *51*, 11814−11818.
(21) Zheng, Y.; Jiao, Y.; Chen, J.; Liu, J.; Liang, J.; Du, A. J.; Zhang, W. M.; Zhu, Z. H.; Smith, S. C.; Jaroniec, M.; Lu, G. Q.; Qiao, S. Z. *J. Am. Chem. Soc.* **2011**, *133*, 20116−20119.
(22) Han, C.; Wang, Y.; Lei, Y.; Wang, B.; Wu, N.; Shi, Q.; Li, Q. *Nano Res.* **2015**, *8*, 1199−1209.
(23) Li, K.; Zeng, X.; Gao, S.; Ma, L.; Wang, Q.; Xu, H.; Wang, Z.; Huang, B.; Dai, Y.; Lu, J. *Nano Res.* **2016**, *9*, 1969−1982.
(24) Liang, Q.; Li, Z.; Bai, Y.; Huang, Z. H.; Kang, F.; Yang, Q.-H. *Sci. China Mater.* **2017**, *60*, 109.
(25) Bai, S.; Ge, J.; Wang, L. L.; Gong, M.; Deng, M. S.; Kong, Q.; Song, L.; Jiang, J.; Zhang, Q.; Luo, Y.; Xie, Y.; Xiong, Y. J. *Adv. Mater.* **2014**, *26*, 5689−5695.
(26) Bai, S.; Li, X. Y.; Kong, Q.; Long, R.; Wang, C. M.; Jiang, J.; Xiong, Y. J. *Adv. Mater.* **2015**, *27*, 3444−3452.
(27) Gong, Y. J.; Lin, J. H.; Wang, X. L.; Shi, G.; Lei, S. D.; Lin, Z.; Zou, X. L.; Ye, G. L.; Vajtai, R.; Yakobson, B. I.; Terrones, H.; Terrones, M.; Tay, B. K.; Lou, J.; Pantelides, S. T.; Liu, Z.; Zhou, W.; Ajayan, P. M. *Nat. Mater.* **2014**, *13*, 1135−1142.
(28) Huang, C. J.; Chen, C.; Zhang, M. W.; Lin, L. H.; Ye, X. X.; Lin, S.; Antonietti, M.; Wang, X. C. *Nat. Commun.* **2015**, *6*, 7698.
(29) Zhang, J. S.; Zhang, G. G.; Chen, X. F.; Lin, S.; Mohlmann, L.; Dolega, G.; Lipner, G.; Antonietti, M.; Blechert, S.; Wang, X. C. *Angew. Chem., Int. Ed.* **2012**, *51*, 3183−3187.
(30) Dong, F.; Zhao, Z. W.; Xiong, T.; Ni, Z. L.; Zhang, W. D.; Sun, Y. J.; Ho, W. K. *ACS Appl. Mater. Interfaces* **2013**, *5*, 11392−11401.
(31) Zhou, Y. J.; Zhang, L. X.; Huang, W. M.; Kong, Q. L.; Fan, X. Q.; Wang, M.; Shi, J. L. *Carbon* **2016**, *99*, 111−117.
(32) Bhattacharyya, S.; Lübbe, M.; Richter, F. *J. Appl. Phys.* **2000**, *88*, 5043−5049.
(33) Zheng, Y.; Jiao, Y.; Zhu, Y. H.; Li, L. H.; Han, Y.; Chen, Y.; Du, A. J.; Jaroniec, M.; Qiao, S. Z. *Nat. Commun.* **2014**, *5*, 3783.
(34) Wu, J.; Liao, L. W.; Yan, W. S.; Xue, Y.; Sun, Y. F.; Yan, X.; Chen, Y. X.; Xie, Y. *ChemSusChem* **2012**, *5*, 1207−1212.
(35) Ray, S. C.; Pao, C. W.; Chiou, J. W.; Tsai, H. M.; Jan, J. C.; Pong, W. F.; McCann, R.; Roy, S. S.; Papakonstantinou, P.; McLaughlin, J. A. *J. Appl. Phys.* **2005**, *98*, 033708.
(36) dos Santos, M. C.; Alvarez, F. *Phys. Rev. B: Condens. Matter Mater. Phys.* **1998**, *58*, 13918−13924.
(37) Yang, F.; Kuznietsov, V.; Lublow, M.; Merschjann, C.; Steigert, A.; Klaer, J.; Thomas, A.; Schedel-Niedrig, T. *J. Mater. Chem. A* **2013**, *1*, 6407−6415.
(38) Martin, D. J.; Reardon, P. J.; Moniz, S. J. A.; Tang, J. W. *J. Am. Chem. Soc.* **2014**, *136*, 12568−12571.
(39) Yan, J. Q.; Wu, H.; Chen, H.; Zhang, Y. X.; Zhang, F. X.; Liu, S. Z. F. *Appl. Catal., B* **2016**, *191*, 130−137.
(40) Liu, G.; Niu, P.; Sun, C. H.; Smith, S. C.; Chen, Z. G.; Lu, G. Q.; Cheng, H. M. *J. Am. Chem. Soc.* **2010**, *132*, 11642−11648.
(41) Ma, X. G.; Lv, Y. H.; Xu, J.; Liu, Y. F.; Zhang, R. Q.; Zhu, Y. F. *J. Phys. Chem. C* **2012**, *116*, 23485−23493.

DOI: 10.1021/jacs.6b11878
J. Am. Chem. Soc. 2017, 139, 3021−3026